



**HAL**  
open science

## Comets beyond 4 au: How pristine are Oort nuclei?

Marco Fulle, M. Lazzarin, F. La Forgia, V. V. Zakharov, I. Bertini, E. Mazzotta Epifani, E. Ammannito, A. Buzzoni, M. T. Capria, A. Carbognani, et al.

► **To cite this version:**

Marco Fulle, M. Lazzarin, F. La Forgia, V. V. Zakharov, I. Bertini, et al.. Comets beyond 4 au: How pristine are Oort nuclei?. Monthly Notices of the Royal Astronomical Society, 2022, 513, pp.5377-5386. 10.1093/mnras/stac1218 . insu-03713295

**HAL Id: insu-03713295**

**<https://insu.hal.science/insu-03713295>**

Submitted on 13 Apr 2023

**HAL** is a multi-disciplinary open access archive for the deposit and dissemination of scientific research documents, whether they are published or not. The documents may come from teaching and research institutions in France or abroad, or from public or private research centers.

L'archive ouverte pluridisciplinaire **HAL**, est destinée au dépôt et à la diffusion de documents scientifiques de niveau recherche, publiés ou non, émanant des établissements d'enseignement et de recherche français ou étrangers, des laboratoires publics ou privés.

# Comets beyond 4 au: How pristine are Oort nuclei?\*

Marco Fulle<sup>1,†</sup>, M. Lazzarin,<sup>2</sup> F. La Forgia<sup>2</sup>, V. V. Zakharov,<sup>3,4</sup> I. Bertini,<sup>3,5</sup> E. Mazzotta Epifani,<sup>6</sup> E. Ammannito,<sup>7</sup> A. Buzzoni<sup>8</sup>, M. T. Capria,<sup>3</sup> A. Carbognani<sup>8</sup>, V. Da Deppo,<sup>9</sup> V. Della Corte,<sup>3</sup> S. Fiscale<sup>5</sup>, E. Frattin,<sup>2</sup> L. Inno<sup>5</sup>, A. Migliorini<sup>3</sup>, C. Pernechele,<sup>10</sup> A. Rotundi,<sup>3,5</sup> G. Sindoni,<sup>7</sup> C. Tubiana<sup>3</sup>, G. Milani,<sup>11</sup> A. Aletti,<sup>11,12</sup> P. Bacci,<sup>11,13</sup> G. Baj,<sup>11</sup> F. Bellini,<sup>11,12</sup> E. Bryssinck,<sup>11,14</sup> M. Di Grazia,<sup>11,13</sup> M. Facchini,<sup>11,15</sup> M. Feraco,<sup>11</sup> E. Guido,<sup>11</sup> R. Ligustri,<sup>11</sup> F. Kugel,<sup>11</sup> M. Maestriperieri,<sup>11,13</sup> D. Tirelli,<sup>11</sup> A. Valvasori,<sup>11,16</sup> C. Snodgrass<sup>17</sup> and G. H. Jones<sup>18,19</sup>

<sup>1</sup>INAF - Osservatorio Astronomico, Via Tiepolo 11, I-34143 Trieste, Italy

<sup>2</sup>Department of Physics and Astronomy ‘G. Galilei’, University of Padova, Vicolo dell’Osservatorio 3, I-35122 Padova, Italy

<sup>3</sup>IAPS - INAF, Via Fosso del Cavaliere 100, I-00133 Rome, Italy

<sup>4</sup>LESIA, Observatoire de Paris, Université PSL, CNRS, 5 place Jules Janssen, F-92195 Meudon, France

<sup>5</sup>Università degli Studi di Napoli Parthenope, Dip. di Scienze e Tecnologie, CDN IC4, I-80143 Naples, Italy

<sup>6</sup>INAF - Osservatorio Astronomico di Roma, Via Frascati 33, Monte Porzio Catone, I-00040 Rome, Italy

<sup>7</sup>Agenzia Spaziale Italiana, Via del Politecnico snc, I-00133 Rome, Italy

<sup>8</sup>INAF - Osservatorio di Astrofisica e Scienza dello Spazio, Via Gobetti 93/3, I-40129 Bologna, Italy

<sup>9</sup>Nat. Res. Council, Inst. for Photonics and Nanotechnologies, Via Trasea 7, I-35131 Padova, Italy

<sup>10</sup>INAF - Osservatorio Astronomico di Padova, Vicolo dell’Osservatorio 5, I-35122 Padova, Italy

<sup>11</sup>CARA Project - INAF - Osservatorio Astronomico di Trieste, Via Tiepolo 11, I-34143 Trieste, Italy

<sup>12</sup>Osservatorio G.V. Schiaparelli, Campo dei Fiori, I-21020 Varese VA, Italy

<sup>13</sup>Osservatorio Astronomico Montagna Pistoiese GAMP, Pian dei Termini, I-51028 San Marcello Pistoiese PT, Italy

<sup>14</sup>Brixia Observatory, 9150 Kruikebe, Belgium

<sup>15</sup>Osservatorio Astronomico Geminiano Montanari, I-41032 Cavezzo (MO), Italy

<sup>16</sup>Osservatorio Felsina AAB, Via Varsellane, 12, I-40050 Monte San Pietro BO, Italy

<sup>17</sup>Institute for Astronomy, University of Edinburgh, Royal Observatory, Edinburgh EH9 3HJ, UK

<sup>18</sup>The Centre for Planetary Sciences at UCL/Birkbeck, London WC1E 6BT, UK

<sup>19</sup>Mullard Space Science Laboratory, University College London, Holmbury St. Mary, Dorking, Surrey RH5 6NT, UK

Accepted 2022 April 25. Received 2022 April 23; in original form 2022 February 12

## ABSTRACT

The ESA mission Comet Interceptor will target an Oort or interstellar comet during its first approach to the Sun. Meanwhile, the Vera Rubin LSST Survey will observe hundreds of active comets per month beyond 4 au from the Sun, where water vapour pressure is expected to be too low to eject dust. We discuss observations of dust tails at heliocentric distances larger than 4 au in order to retrieve the physical parameters driving cometary activity beyond Jupiter by means of a probabilistic tail model, which is consistent with the activity model defining the gas coma parameters due to the sublimation of carbon monoxide, molecular oxygen, methane, ethane, and carbon dioxide since the activity onset at 85 au from the Sun. We find that: (i) All the observed dust tails are consistent with the adopted activity model; (ii) The tail fits depend on three free parameters only, all correlated to the nucleus size; (iii) Tail fits are always improved by anisotropic dust ejection, suggesting activity of Oort nuclei dominated by seasons; (iv) Inbound seasons suggest cometary activity before the ejection of protocomets into the Oort cloud, as predicted by the activity model; (v) Oort nuclei larger than 1 km may be characterized by a fallout up to  $\approx 100$  m thick deposited during  $\approx 60$  yr inbound; (vi) On the other side, Oort nuclei smaller than 1 km may appear more pristine than Jupiter Family Comets when observed at 1 au from the Sun.

**Key words:** space vehicles – comets: general – Oort Cloud – protoplanetary discs.

## 1 INTRODUCTION

The ESA mission Comet Interceptor will target an Oort or interstellar comet during its first approach to the Sun at the heliocentric distance  $r_h \approx 1$  au (Snodgrass & Jones 2019). In order to optimize the mission, whose plan will require months to years between the target discovery and the flyby, it is mandatory to understand how cometary activity

† E-mail: marco.fulle@inaf.it

\* In memory of our colleague and friend Maria Teresa Capria, who passed away on 2022 April 14

evolves during the inbound orbit from the outer Solar System, where it is driven by the sublimation of ices more volatile than water-ice (the so-called supervolatiles), to the inner Solar System, where it is also driven by water.

In order to accomplish this goal, we have started a long-term program of observations of dust tails of Oort comets approaching the Sun and active before the water-driven activity onset, probably occurring at  $r_h \approx 3.8$  au (Fulle et al. 2020b; Ciarniello et al. 2021). Such a water-activity onset is consistent with the activity of Jupiter Family Comets observed at  $r_h > 3$  au (Kelley et al. 2013). Three of these comets were observed to be active at  $r_h < 3.5$  au. Other six comets have their perihelion at  $r_h > 3.6$  au, implying an activity driven by some supervolatile (probably CO<sub>2</sub>) over all their orbit. The remaining seventeen comets show only outbound activity at  $r_h \leq 5.7$  au, best explained by a post-perihelion bound dust coma (Bertini et al. 2019) evolving in a fallout lasting many months (Ciarniello et al. 2022) and in a fossil tail.

Besides investigating how comets evolve before the onset of water-driven activity, one of our aims is to test the robustness and possible automation of the probabilistic tail model already successfully applied to the dust tail of interstellar comet 2I/Borisov (Cremonese et al. 2020), in view of its application to the data set of the Legacy Survey of Space and Time (LSST) at the Vera Rubin Observatory (Jones et al. 2020). The survey will probably monitor hundreds of dust tails driven by supervolatiles per month, thus providing the best possible statistics to test which parameters drive cometary activity and tails. We discuss here the results obtained after one year of observations at the Italian National Telescope (TNG at La Palma, Canary Islands), aimed to characterize the statistics of cometary activity driven by supervolatiles.

## 2 PROBABILISTIC TAIL MODEL

Decades of investigations of cometary dust have shown that both sizes and porosity of the dust particles cover huge ranges of values (Güttler et al. 2019). In particular, dust porosity may cover all values from zero, namely rocks probably formed close to our protosun (Brownlee et al. 2006), to almost one, namely fractals formed in the protosolar nebula (Fulle & Blum 2017). Both the motion of dust in the coma under the action of gas drag, and in the tail under the action of solar radiation pressure, depend on the quantity  $\rho_d s$ , where the dust bulk density  $\rho_d$  and the dust size  $s$  cover similar huge ranges of values, due to the porosity dispersion. Dust tails are best parametrized by the ratio between the solar radiation pressure force and the solar gravity force

$$\beta = C_{\text{pr}} Q_{\text{pr}} (\rho_d s)^{-1}, \quad (1)$$

where  $C_{\text{pr}} = 1.19 \times 10^{-3} \text{ kg m}^{-2}$  and  $Q_{\text{pr}} \approx 1$  for the particles usually observed in dust tails (Fulle et al. 2010). It is therefore impossible to convert  $\beta$  to sizes and vice-versa, or to parametrize dust coma models by sizes only, because each dust trajectory both in comae and in tails occurs for an infinite combination of possible dust bulk densities and sizes. Conversely, we can define the probability distribution of the  $\beta$  values, when the probability distributions of dust bulk densities and sizes are known. Data of dust bulk density collected by the ESA mission Rosetta (Fulle et al. 2017) and models of water-driven activity (Fulle et al. 2020b) suggest that the  $\beta$ -distribution is a lognormal distribution centred at  $\beta_0 = 5 \times 10^{-4}$  and characterized by the dispersion  $\sigma$  (Cremonese et al. 2020).  $\sigma$  is the first free parameter of the probabilistic tail model, convoluting both dust (porosity) and nucleus (how dust is ejected) physical properties.

Models of cometary tails are obtained by means of Monte Carlo integration of  $3 \times 10^8$  particles following 3D heliocentric orbits fixed by the  $\beta$ -parameter and by the ejection velocity vector of absolute value  $v_d$  at  $r_h = 10$  au and  $\beta = \beta_0$ , namely the second free parameter of the probabilistic tail model. The fit of the coma brightness provides the dust loss rate of value  $Q_d$  at  $r_h = 10$  au. The dust loss rate depends on  $r_h^{-k}$ , where  $k$  is the third free parameter of the probabilistic tail model. In the next section, we show that the adopted activity model provides the onset of dust ejection and the  $r_h$ -dependence of the gas temperature and loss rate. These gas parameters allow us to compute the  $r_h$ -dependence of the dust velocity. The  $r_h$ -dependence of the dust loss rate depends on the amount of dust fallout on the nucleus, which cannot be predicted by the activity model because it depends on the nucleus shape, spin state and seasons, not constrained by the available ground-based observations.

Available data of Interplanetary Dust Particles and of the dust collected at comet 81P/Wild 2 by the Stardust mission and at comet 67P/Churyumov-Gerasimenko by the Rosetta mission suggest that all comets eject dust of similar structure (Güttler et al. 2019). The adopted activity model fits available data of comets 67P, 103P/Hartley 2 (Fulle 2021) and 2I/Borisov (Cremonese et al. 2020), suggesting that it can be applied to Oort comets too. Tail fits of good quality will allow us to conclude that the parameters fixed by the adopted activity model have second-order effects in shaping the observed comae and tails with respect to the tuned free parameters  $v_d$ ,  $\sigma$  and  $k$ . Since our goal is the automation of tail fits, it is mandatory to minimize the number of free parameters of the probabilistic tail model.

## 3 ACTIVITY MODEL BEYOND 4 AU

Most thermophysical models of nuclei rely on the assumption of dry mantles (where water-ice sublimation is assumed to be negligible) enveloping nuclei rich in ices (Keller et al. 2015; Davidsson et al. 2022). However, a dry crust or mantle where water-ice sublimation is assumed to be negligible is inconsistent with the definition itself of a comet, i.e. a nucleus surrounded by a gas and dust coma, because the gas pressures at the mantle surface are always lower than the tensile strengths bonding the dust particles among them, according to laboratory experiments (Skorov & Blum 2012; Blum et al. 2014; Gundlach et al. 2015; Brisset et al. 2016), unless unrealistic parameters are assumed, e.g. a metre-thick mantle depleted of supervolatiles and with pores of sizes  $\leq 1$  mm (Bouziani & Jewitt 2022), inconsistent with water-driven activity at  $r_h < 3.8$  au and with the ejection of dm-sized chunks from Jupiter Family Comets (Kelley et al. 2015; Fulle et al. 2016; Ott et al. 2017; Gundlach et al. 2020). Also the observed evolution of the nucleus colour of Comet 67P/Churyumov-Gerasimenko excludes the presence of any ices-depleted crust (Ciarniello et al. 2022). Models based on a crust where water-ice sublimation is assumed to be negligible (Davidsson et al. 2022) are inconsistent with the measured 67P Hapi's erosion (Cambianica et al. 2020), so that they cannot constrain the nucleus refractory-to-water-ice mass ratio  $\delta_w$ . They also require ad-hoc changes of the thickness of the dry crust enveloping the entire nucleus (Skorov et al. 2020) to fit the observed time evolution of the gas loss rates (Läuter et al. 2020). The thickness of the crust where water-ice sublimation is assumed to be negligible ranges from a few tens of  $\mu\text{m}$  (Keller et al. 2015) to a metre (Bouziani & Jewitt 2022) according to the specific fit of each single observation.

Only recently a nucleus thermophysical model consistent both with dust ejection and with all available data of cometary dust (Güttler

**Table 1.** Ice parameters.  $\Delta T$ : Temperature range (K) where the gas pressure from the sublimating ice is  $P = P_0 \exp(-T_0/T)$  Pa; within  $\Delta T$ , ethane crosses the triple point.  $\Lambda$ : Latent heat of sublimation ( $\text{J kg}^{-1}$ ). References: 1, Fray & Schmitt (2009); 2, Huebner et al. (2006); 3, Ahern & Lawson (1968); 4, Stephenson & Melinowski (1987); 5, Regnier (1972); 6, Gundlach et al. (2020).

Ice	$\Delta T$	$P_0$	$T_0$	$\Lambda$	Ref.
CO	$30 < T < 50$	$1.73 \times 10^{10}$	942	$2.3 \times 10^5$	1, 2
O <sub>2</sub>	$40 < T < 50$	$1.37 \times 10^{10}$	998	$2.9 \times 10^5$	1, 3
CH <sub>4</sub>	$50 < T < 70$	$5.45 \times 10^9$	1182	$6.1 \times 10^5$	1, 4
C <sub>2</sub> H <sub>6</sub>	$80 < T < 100$	$1.44 \times 10^{12}$	2520	$7.5 \times 10^5$	1, 5
CO <sub>2</sub>	$100 < T < 160$	$2.89 \times 10^{12}$	3271	$5.7 \times 10^5$	6

et al. 2019) has been developed (Fulle et al. 2020b). It shows that the only parameter-free approach overcoming the tensile strength bonding the dust particles to the nucleus surface is ice sublimation occurring inside the particles themselves, because only this process provides a gradient of the gas pressure much steeper than in any crust where ice sublimation is assumed to be negligible. This model, applied to water–ice sublimation, fits most collected data at 67P (Fulle et al. 2020b; Fulle 2021), e.g. the measured Hapi’s erosion and the 67P water loss rate observed by *Rosetta* from 2014 to 2016 without the assumption of any free parameter (Ciarniello et al. 2021). It also predicts the anticorrelation between the deuterium-to-hydrogen ratio (D/H) and the hyperactivity of comets (Lis et al. 2019; Fulle 2021). Recent estimates of the 67P D/H at perihelion (Müller et al. 2022) perfectly match the predicted value in case of negligible water distributed sources (Fulle 2021). The model confirms that nuclei of comets are composed of cm-sized pebbles (Blum et al. 2017), which are inhomogeneous clusters of porous dust particles, i.e. porous agglomerates of rocks and ice-enveloped dust grains (Güttler et al. 2019). The same model applied to CO-ice sublimation is consistent with ejection of mm-sized dust since  $r_h = 85$  au (Fulle, Blum & Rotundi 2020a).

Here we extend such an activity model to all ices more volatile than water-ice, each characterized by its refractory-to-ice mass ratio  $\delta_i$ . The sublimation of the ice driving dust ejection occurs close to the nucleus surface, whereas all other ices sublimate at different depths, i.e. at temperatures much lower than the surface one. Then, the gas flux from the ice driving dust ejection is larger than all others, independent of the actual abundance of the ices in the nucleus, which may be different than the molecular abundances measured in comae (Rubin et al. 2020). Here we make the following assumptions for all the considered ices in the nucleus: (i) their fraction trapped in other ices and clathrates is negligible (Balucani et al. 2015); (ii) they are present as pure ices thus sublimating beyond the water activity onset, namely  $r_h > 3.8$  au (Fulle et al. 2020b; Ciarniello et al. 2021), and (iii) the values of  $\delta_w$  and  $\delta_i$  provide

$$\frac{1}{1 + \delta_w} + \sum_i \frac{1}{1 + \delta_i} < \frac{1}{3}, \quad (2)$$

where the subscript  $i$  runs over all the considered ices of super-volatiles (Table 1). The quantity  $(1 + \delta_i)^{-1}$  is an upper limit of each ice mass fraction, so that equation (2) ensures us that the total volume fraction of all ices is lower than that of refractories. This condition is consistent with ices embedded inside the dust particles, forcing the gas sublimating from all ices to diffuse through the micropores of porous dust particles composing the nucleus (Fulle et al. 2020b). If all ices sublimate inside porous dust on the surface of nuclei, then nuclei of comets are necessarily composed of cm-sized

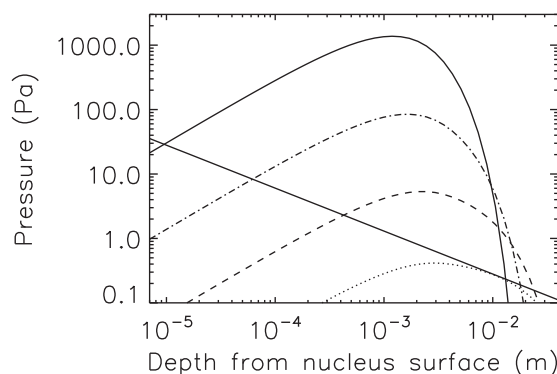


**Figure 1.** Pressure  $P$  of CO<sub>2</sub> gas inside the pebbles versus the depth  $s$ . Continuous straight line: tensile strength,  $S$ , bonding a dust homogeneous aggregate of size  $s$  (Skorov & Blum 2012). Continuous curved line:  $P$  at  $T_s = 160$  K and  $\nabla T = 39 \text{ K cm}^{-1}$  crosses  $S$  at  $s_m = 9 \mu\text{m}$  and  $s_M = 12 \text{ mm}$ , where  $s_m$  and  $s_M$  are the minimum and maximum sizes of the ejected dust. Dot and dashed line:  $P$  at  $T_s = 139$  K and  $\nabla T = 17 \text{ K cm}^{-1}$  crosses  $S$  at  $s_m = 60 \mu\text{m}$  and  $s_M = 2 \text{ cm}$ . Dashed line:  $P$  at  $T_s = 123$  K and  $\nabla T = 7 \text{ K cm}^{-1}$  crosses  $S$  at  $s_m = 0.4 \text{ mm}$  and  $s_M = 25 \text{ mm}$ . Dotted line: the curve  $P$  at  $T_s = 111$  K and  $\nabla T = 2 \text{ K cm}^{-1}$  is tangent to the line  $S$  at  $s_m = s_M = 1 \text{ cm}$ .

pebbles (Fulle, Blum & Rotundi 2019), as assumed in the following equations.

At each heliocentric distance  $r_h$ , the activity model (Fulle et al. 2020b) is defined by five analytical equations fixing (i) the gas pressure  $P(s)$  depending on the depth  $s$  from the nucleus surface (Fig. 1 for the CO<sub>2</sub> case), (ii) the gas flux  $Q$  from the nucleus surface, (iii) the temperature gradient  $\nabla T$  at depths of a few cm, (iv) the heat conductivity  $\lambda_s$  at depths of a few cm below the nucleus surface, and (v) the temperature  $T_s$  of the nucleus surface

$$P(s) = P_0 f(s) \exp \left[ -\frac{T_0}{T_s - s \nabla T} \right] \quad (3)$$

$$Q = \frac{14 r P(R)}{3 R} \sqrt{\frac{2 m}{\pi k_B (T_s - R \nabla T)}} \quad (4)$$

$$\nabla T = \frac{\sqrt{\Lambda Q / \sigma_B}}{8 (T_s - R \nabla T) R} \quad (5)$$

$$\lambda_s = \frac{32}{3} (T_s - R \nabla T)^3 \sigma_B R \quad (6)$$

$$(1 - A) I_\odot \cos \theta r_h^{-2} = \epsilon \sigma_B T_s^4 + \lambda_s \nabla T + \Lambda Q, \quad (7)$$

where  $P_0$ ,  $T_0$ , and  $\Lambda$  values are listed in Table 1,  $s$  is the depth from the nucleus surface,  $f(s) = 1 - (1 - \frac{s}{R})^4$  for  $s \leq R$ ,  $f(s) = 1$  elsewhere,  $r \approx 50 \text{ nm}$  and  $R \approx 5 \text{ mm}$  are the radii of the grains of which cometary dust consists (Levasseur-Regourd et al. 2018; Güttler et al. 2019; Mannel et al. 2019) and of the pebbles of which cometary nuclei consist (Blum et al. 2017; Fulle et al. 2020b),  $m$  is the mass of the gas molecule,  $k_B$  is the Boltzmann constant,  $\sigma_B$  is the Stefan–Boltzmann constant,  $A$  is the nucleus Bond albedo (e.g.  $A = 1.2$  per cent measured at 67P; Fornasier et al. 2015),  $I_\odot$  is the solar flux at the heliocentric distance of Earth,  $\theta$  is the solar zenithal angle, and  $\epsilon \approx 0.9$  is the nucleus emissivity. Since the gas originates from the superficial pebbles and is assumed to share the temperature  $T_s - s \nabla T$  of refractories and ices, the thermal diffusion due to gas convection is negligible with respect to the sublimation sink  $\Lambda Q$ . A nucleus is active if the gas pressure overcomes the tensile strength  $S$  bonding dust particles to the nucleus surface (Skorov & Blum 2012), thus defining the activity onset for each ice (Table 2), occurring (i) at  $r_h = 85$  au for carbon monoxide (Fulle et al. 2020a); (ii) at  $r_h = 60$

**Table 2.** Activity parameters.  $r_h$ : Heliocentric distance (au, Sun at zenith and nucleus Bond albedo  $A = 1.2$  per cent).  $T_s$ : Nucleus surface temperature (K), equation (7).  $\nabla T$ : Temperature gradient at depths of a few cm ( $\text{K cm}^{-1}$ ), equation (5).  $\lambda_s$ : Nucleus heat conductivity ( $\text{W m}^{-1} \text{K}^{-1}$ ) at the depth  $R = 5$  mm, equation (6).  $P$ : Gas pressure at the depth  $R$  (Pa), equation (3).  $Q$ : Gas flux from the nucleus surface ( $\text{kg m}^{-2} \text{s}^{-1}$ ), equation (4).  $E$ : Nucleus erosion rate ( $\text{mm day}^{-1}$ ).  $\delta_i$ : Upper limit of the refractory-to-ice mass ratio, equation (8).  $s_c$ : Size of the chunks (mm) ejected by the ice (within brackets) sublimating at the depth  $s_c$  with gas pressure  $S$ .  $v_g$ : Maximum terminal gas velocity ( $\text{m s}^{-1}$ ).  $v_d$ : Maximum terminal dust velocity ( $\text{m s}^{-1}$ ) at the reference value  $\beta_0$  assuming no gravity by a nucleus of radius  $R_n = 1$  km (Zakharov et al. 2018, 2021).

Ice	$r_h$	$T_s$	$\nabla T$	$\lambda_s$	$P(R)$	$Q$	$E$	$250 r_h^{-1}$	$\delta_i$	$s_c$	$v_g$	$v_d$	$20 r_h^{-1}$
CO	85	40	4	$1.7 \times 10^{-4}$	0.3	$10^{-7}$	6	3	–	–	279	0.25	0.24
CO	60	44	7	$1.9 \times 10^{-4}$	1.3	$3.4 \times 10^{-7}$	2	4	35	13 ( $\text{N}_2$ )	293	0.47	0.33
$\text{O}_2$	60	44	5	$2.2 \times 10^{-4}$	0.4	$1.4 \times 10^{-7}$	8	4	–	–	280	0.29	0.33
$\text{O}_2$	52	47	8	$2.4 \times 10^{-4}$	1.1	$3.5 \times 10^{-7}$	3	5	45	12 ( $\text{CO}$ )	283	0.47	0.38
$\text{CH}_4$	52	52	3	$3.8 \times 10^{-4}$	0.4	$10^{-7}$	14	5	–	–	450	0.31	0.38
$\text{CH}_4$	18	68	20	$5.9 \times 10^{-4}$	7.7	$2.0 \times 10^{-6}$	6	14	20	14 ( $\text{O}_2$ )	520	1.48	1.11
$\text{C}_2\text{H}_6$	18	89	3	$2.0 \times 10^{-3}$	0.4	$10^{-7}$	30	14	–	–	450	0.30	1.11
$\text{C}_2\text{H}_6$	13	98	5	$2.6 \times 10^{-3}$	5.0	$1.2 \times 10^{-6}$	18	19	120	100 ( $\text{CH}_4$ )	472	1.08	1.54
$\text{CO}_2$	13	111	2	$4.0 \times 10^{-3}$	0.4	$10^{-7}$	43	19	–	–	371	0.29	1.54
$\text{CO}_2$	9.2	123	7	$5.2 \times 10^{-3}$	4.2	$10^{-6}$	22	27	–	57 ( $\text{C}_2\text{H}_6$ )	391	0.93	2.22
$\text{CO}_2$	6.3	139	17	$6.6 \times 10^{-3}$	34.	$8.1 \times 10^{-6}$	33	40	–	–	428	2.76	3.17
$\text{CO}_2$	3.8	160	39	$8.3 \times 10^{-3}$	200	$4.7 \times 10^{-5}$	90	66	10	19 ( $\text{C}_2\text{H}_6$ )	445	6.75	5.26

au for molecular oxygen; (iii) at  $r_h = 52$  au for methane; (iv) at  $r_h = 18$  au for ethane; (v) at  $r_h = 13$  au for carbon dioxide (dotted line in Fig. 1); and (vi) at  $r_h = 3.8$  au for water (Fulle et al. 2020b; Ciarniello et al. 2021). The value  $R \approx 5$  mm has been constrained by several data collected at comet 67P, by laboratory experiments of dust accretion in conditions expected to occur in the solar protoplanetary disc and by observations of other protoplanetary discs (Blum et al. 2017). Other  $R$ -values would not provide the best fit of the 67P water-loss time-evolution (Ciarniello et al. 2021).

Cometary activity is driven by the gas pressure  $P(s)$ , which does not depend on the ice abundance, but only on the gas temperature: also minor species can drive cometary activity, provided that heat transfer inside a pebble is faster than ice depletion. This condition fixes an upper limit for the refractory-to-ice mass ratio  $\delta_i$  (Fulle 2021)

$$\delta_i < \frac{\lambda_s}{3 Q R c_p} - 1, \quad (8)$$

where  $c_p \approx 10^3 \text{ J kg}^{-1} \text{ K}^{-1}$  is the heat capacity of the pebbles (Blum et al. 2017). In order to fulfil equation (2) during the whole inbound orbit, cometary activity is driven by at least the five ices listed in Table 2, reporting the nucleus and gas coma parameters computed by means of the activity model (Fulle et al. 2020b). Thus, the less abundant the ice, the shorter the  $r_h$ -range where it can drive cometary activity (e.g. ethane in Table 2). The upper limit of each water-to-ice mass ratio is  $\delta_i/\delta_w$ , and in the protoplanetary disc  $\delta_w \approx 5$  (Cambianica et al. 2020). The probable activity due to further ices not listed in Table 2 and the decrease of  $c_p$  with the temperature (Takahashi & Westrum 1970; Shulman 2004; Bouziani & Jewitt 2022) significantly increase the upper limits of  $\delta_i$ . However, e.g. formaldehyde has unknown thermodynamical parameters (Fray & Schmitt 2009), and e.g. ethylene and nitric oxide were not detected in 67P (Rubin et al. 2020), thus preventing a realistic computation of e.g. evolving  $c_p$  values. According to the activity model, the distribution of water-ice is very inhomogeneous in the nucleus (Ciarniello et al. 2022), with water-rich pebbles, depleted of supervolatiles, embedded in a matrix of water-poor pebbles, which are rich of the ices listed in Table 2. Therefore, at  $r_h > 3.8$  au, dust is ejected from water-poor pebbles only, characterized by  $\delta_w \approx 50$  (Fulle 2021), so that equation (2) is surely verified. In water-poor pebbles the water ice is less abundant than all other ices (excluded ethane, Table 2), so that

these ices cannot be trapped inside a less abundant water ice. The observed activity of C/2017K2 at  $r_h = 23.7$  au (Jewitt et al. 2017) excludes also that ices may be trapped inside  $\text{CO}_2$ -ice, because the  $\text{CO}_2$ -driven activity onsets at  $r_h = 13$  au (Table 2).

At the activity onset of each ice, the ice, that was driving the activity before, migrates to nucleus depths  $> 2R$ , because the new surface temperature and thermal gradient shift its sublimation front to the depth  $s_c$  (Table 2). While the comet approaches to the Sun, the gas flux  $Q$  increases faster than the heat conductivity  $\lambda_s$ , so that the upper limit of  $\delta_i$ , input in equation (2), is computed when the activity shifts from one gas to the other (Table 2). All the parameters listed in Table 2 are computed with the Sun at zenith, so that the heliocentric distance of the activity onset decreases as the solar zenithal angle increases. According to the actual solar zenithal angle of each nucleus facet at each heliocentric distance  $r_h$ , all the ices having the activity onset at a heliocentric distance larger than  $r_h$  continue to drive the dust ejection, thus smearing the discontinuities of all the gas and dust coma parameters computed at each activity onset (Table 2). Our model predicts that Oort comets at  $r_h \approx 1$  au may still eject sub-cm dust by the pressure of supervolatiles in the superficial pebbles, according to the nucleus seasons. On the other hand,  $\text{CO}_2$ -driven activity in Jupiter Family Comets can eject dm-sized chunks only, because the  $\text{CO}_2$ -ice sublimation front is expected at depths of  $\approx 0.1$  m (Fulle et al. 2020b; Gundlach et al. 2020). According to these models of Jupiter Family comets, sub-cm dust is always ejected by water-driven activity, intermixed with  $\text{CO}_2$ -driven activity close to perihelion (Ciarniello et al. 2021, 2022).

At each heliocentric distance, the nucleus is eroded into dust of size  $s_m \leq s \leq s_M$  (Fig. 1 for the  $\text{CO}_2$  case) by the gas sublimating in the superficial pebbles from the ice listed in the first column of Table 2, and into chunks of size  $s_M < s \leq s_c$  by the gas sublimating at the depth  $s_c$  from the ice listed in the same column, Table 2. Such an activity is analogous to the water-driven one of 67P, with  $\text{CO}_2$  gas ejecting dm-sized chunks because  $\text{CO}_2$ -ice sublimation occurs at that depth (Gundlach et al. 2020). The nucleus erosion rate  $E$  depends on  $s_M$  and, opposite to the nucleus ice depletion rate  $D$ , is independent of  $\delta_i$  (Fulle et al. 2020b). For  $r_h > 15$  au,  $s_M \leq 2R$  for all the considered ices, so that always  $D < E$ . The ejected chunks behave differently with respect to the water-poor ones ejected at 67P perihelion, which have  $\delta_w \approx 50$ , do not fulfil equation (8) and are thus inactive (Fulle 2021). Chunks ejected at  $r_h > 15$  au are eroded into sub-cm dust,

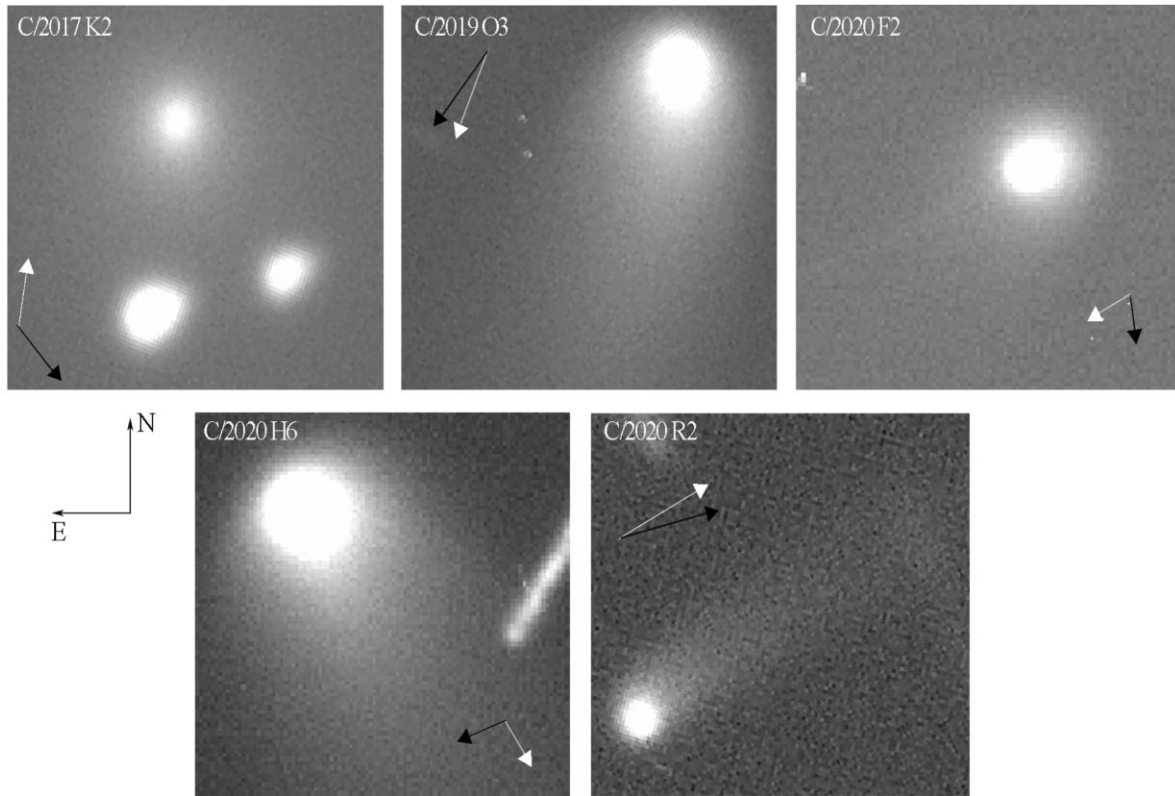


**Figure 2.** Images of the dust tails summarized in Table 3. Each image covers a field of view of  $25'' \times 25''$ . Black arrow: antisolar direction. White arrow: Trailing orbit direction.

**Table 3.** Tail observations.  $q$ : Perihelion heliocentric distance (au).  $e$ : Eccentricity of orbit. Exp.: Exposure time (s).  $r_h$ : Sun-comet distance (au).  $\Delta$ : Earth-comet distance (au).  $\phi$ : Sun-comet-Earth phase angle (deg).

Comet	$q$	$e$	Perihelion UT	Observation UT	Exp.	$r_h$	$\Delta$	$\phi$
C/2017K2	1.7995	1.00041	2022 Dec 19.99	2021 May 17.08	180	6.354	5.968	8.7
C/2019O3	8.8195	1.00199	2021 Mar 07.70	2021 Aug 07.02	1200	8.863	8.548	6.4
C/2020F2	8.8168	1.00257	2022 Jul 16.68	2021 May 07.17	1400	9.169	8.169	0.9
C/2020H6	4.7029	1.00082	2021 Oct 01.05	2021 May 07.10	1200	4.844	3.867	3.3
C/2020R2	4.6923	0.98863	2022 Feb 24.28	2021 Oct 03.21	1800	4.828	3.876	4.1

with rocket effects by the lost gas pushing them into the innercoma night side. The activity model thus predicts gradients of the coma dust density along the sunward-to-antisunward direction lower than in the direction perpendicular to the comet orbital plane, and dust deposits composed of sub-cm particles rather than chunks (Pajola et al. 2017). These deposits may still contain ices (Fulle 2021), so that they may be active in the outbound orbit and during other few perihelion passages, according to the nucleus seasons. Only  $\text{CO}_2$  gas reaches pressures inside the superficial pebbles comparable to the water-vapour one at  $r_h < 3$  au. For  $r_h > 10$  au, all gas pressures are lower than the water-vapour one at  $r_h < 3$  au. For  $r_h > 10$  au, the activity model thus predicts  $\sigma$  values lower than observed in water-driven dust tails (Cremonese et al. 2020), both because  $s_m > 0.4$  mm and because all chunks are eroded into sub-cm dust in the inner coma.

The gas parameters  $Q$  and  $T_x$  (Table 2) are used as input for gas and dust 1D coma models (Zakharov et al. 2018) to compute the gas and dust maximum terminal velocities  $v_g$  and  $v_d$  at the reference value  $\beta_0$ . The dependence on the heliocentric distance of both the nucleus erosion  $E$  and dust maximum terminal velocity

$v_d$  is best approximated by  $r_h^{-1}$  (Table 2), and this dependence is considered as input in the probabilistic tail model. For  $9 < r_h < 13$  au, the  $\text{CO}_2$ -driven velocities are lower than the adopted interpolation. However, above the nucleus facets of large solar zenithal angles the dust velocity is driven by ethane and methane, dragging the dust to velocities up to  $v_d = 1.5$  m s $^{-1}$ , consistent with the adopted interpolation. For  $r_h > 20$  au, the dust terminal velocity is lower than the escape velocity from the nucleus gravity field, thus implying large dust fallout on the nucleus, making the dust loss rate steeper than the erosion rate. Therefore  $k \geq 1$ , with  $k = 1$  for small fallouts independent of  $r_h$ . For  $r_h > 20$  au, visible tails become much less probable than unresolved sub-pixel bound comae around the nucleus, suggesting that nucleus size estimates based on the nucleus magnitudes or point-spread functions may be significantly overestimated.

The photometric quantity  $Af\rho$  (A'Hearn et al. 1984) is linked to the dust loss rate  $Q_d$  by

$$Q_d = C_q v_d A f \rho, \quad (9)$$

where  $C_q = 20 \text{ kg m}^{-2}$  (Cremonese et al. 2020), and thus depends on  $r_h^{1-k}$ . The dust velocities scale as  $\sqrt{R_n}$ , where  $R_n$  is the nucleus radius [equation (29) in Zakharov et al. (2021)], where the gas loss rate is proportional to  $R_n^2 Q$ . It follows that the three free parameters of the probabilistic model of tails observed at  $4 < r_h < 10 \text{ au}$  are all correlated to  $R_n$ : the larger  $R_n$ , the larger  $v_d$  (proportional to  $\sqrt{R_n}$ ), the larger  $k$  (i.e. the fallout because the nucleus is bigger), the larger the fraction of dust ejected by  $\text{CO}_2$ -driven activity in the tail, the larger  $\sigma$  (because  $\text{CO}_2$ -driven activity ejects dust of sizes covering wider ranges than other supervolatiles).

#### 4 OBSERVATIONS OF TAILS

Tails of comets beyond 4 au from the Sun were observed with the 3.58 m Telescopio Nazionale Galileo (TNG), located at the Roque de los Muchachos Observatory, La Palma, according to the proposal ‘Spectroscopic investigation of Dynamically New Comets as background for the ESA Comet Interceptor mission’ approved for the allocation times AOT41-44. Images were acquired in the  $R$  band on 2021 with the Device Optimized for the LOw RESolution (DOLORES) instrument. DOLORES carries a  $2048 \times 2048 \text{ E2V-4240 CCD}$  with a field of view of  $8'.6 \times 8'.6$ , giving a scale of  $0.252 \text{ arcsec pixel}^{-1}$ . A summary of the observations, heliocentric, and geocentric distances to the comets, and their phase angles are reported in Table 3. Correction of the raw data for bias, overscan, and flat-field was performed using standard IRAF routines. Fig. 2 shows the images of the observed tails.

#### 5 COMA PHOTOMETRY

Photometric data of comets C/2017K2, C/2019O3, and C/2020H6 were obtained with the Cassini 152-cm telescope at the Loiano Observatory (INAF-OAS), Italy. The telescope camera is equipped with a  $1340 \times 1300 \text{ pixels CCD}$  with a scale of  $0.568 \text{ arcsec pixel}^{-1}$ , yielding a total field of view of  $12'.7 \times 12'.3$ . Images were taken in the broad-band  $R$ -Johnson filter. Calibrating frames were obtained for the usual bias subtraction and flat-field normalization. A proper sky subtraction was performed measuring the sky statistics close but not adjacent to the comets, avoiding contamination effects from their coma and tail. During photometric nights, images of photometric standard stars in Landolt fields (Landolt 2009) were taken to perform the absolute flux calibration of our frames. Atmospheric extinction coefficients were derived with the method of Bouguer’s lines using a single standard star field images at different air masses.

When nights were not perfectly photometric, we preferred to derive an absolute calibration performing differential photometry with catalogue stars identified in the comets frames, since atmospheric extinction is difficult to correct in atmospheric inhomogeneous conditions. In order to identify field stars with known  $R$  magnitude, we used the University of Strasbourg Vizier online service (<https://vizier.u-strasbg.fr/viz-bin/VizieR>) and the Fourth U.S. Naval Observatory CCD Astrograph UCAC4 Catalogue (Zacharias et al. 2013). We therefore derived appropriate calibration factors between instrumental and catalogue magnitudes. In differential photometry attention must be paid to the conversion of the used catalogue photometric system into the system used by Landolt, in order to have consistent data derived from this methodology compared to the ones coming from the classical reduction method with standard stars. The UCAC4 catalogue contains star magnitudes in the AAVSO Photometric All-Sky Survey (APASS) system which is composed by Johnson-B, Johnson-V, and Sloan  $r$  magnitudes (Henden et al. 2016). The catalogue stars  $r$  magnitudes were converted into the

**Table 4.**  $Af\rho$  measurements.  $r_h$ : Heliocentric distance (au).  $Af\rho$ : Coma brightness (m) measured within the coma sky-projected radius  $\rho_0$  ( $10^4 \text{ km}$ ). The measurements of C/2017K2 by Loiano Observatory and the CARA network (all with  $\rho_0 = 5 \times 10^4 \text{ km}$ ) are reported in Fig. 3. Values of  $\rho_0 < 5 \times 10^4 \text{ km}$  are adopted when stars pollute the coma or the coma has a smaller radius.

Comet	$r_h$	$Af\rho$	$\rho_0$	Observatory
C/2017K2	6.354	$90 \pm 3$	$2.5 \pm 1.0$	TNG
C/2019O3	8.837	$52 \pm 7$	5	Brixiiis
C/2019O3	8.847	$49 \pm 2$	$2.0 \pm 0.8$	Loiano
C/2019O3	8.853	$43 \pm 6$	5	Brixiiis
C/2019O3	8.854	$63 \pm 9$	5	Brixiiis
C/2020F2	9.169	$30 \pm 5$	$2.0 \pm 1.5$	TNG
C/2020H6	4.751	$7.2 \pm 0.3$	$1.2 \pm 0.5$	Loiano
C/2020H6	4.783	$7.6 \pm 1.0$	5	Brixiiis
C/2020H6	4.791	$7.6 \pm 1.0$	5	Brixiiis

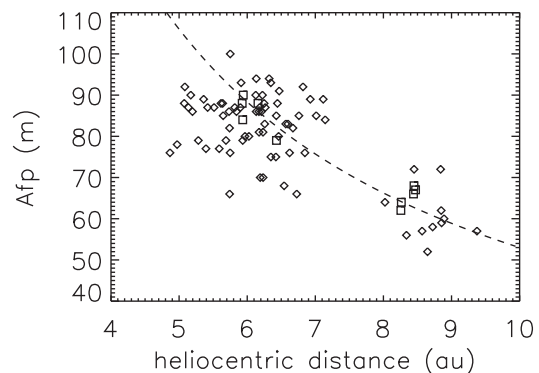


**Figure 3.**  $Af\rho$  of comet C/2017K2 versus the heliocentric distance  $r_h$  measured within a sky-projected coma radius  $\rho_0 = 5 \times 10^4 \text{ km}$ . Diamonds: observations of the CARA network. Squares: observations at Loiano Observatory. Dashed line: best fit of Loiano’s data constrained by the dust tail model (Table 5).

corresponding  $R$  magnitudes used by Landolt (Dymock & Miles 2018) according to  $R = r - 0.108 (B-V) - 0.132$ . This formula was found to be valid in the range  $9 < R < 16$  and we considered catalogue stars of magnitude falling in this range.

The  $Af\rho$  parameter was then derived at different cometocentric distances measuring the calibrated flux in the correspondent photometric aperture and considering the solar flux in the same filter. The solar flux term was obtained from the Sun apparent magnitude  $V_{\text{Sun}} = -26.74$  (Meech et al. 2013) and the solar colours (Holmberg, Flynn & Portinari 2006), yielding a final apparent  $R_{\text{Sun}} = -27.094$ . Moreover, we performed an additional test measuring the  $Af\rho$  parameter and the comet magnitude with differential photometry also in photometric nights, comparing then the results with the ones derived from usual standard stars calibration. We found the two methodologies consistent within 10 per cent for  $Af\rho$  results, being this the largest measured difference. This result gave us confidence in properly comparing the measurements coming from the two methods (Table 4 and Fig. 3). Differential photometry was also applied to TNG data (Table 3) when UCAC4 stars available in the observation field were not saturated, and is usually adopted by the CARA network (Fulle et al. 2010; Cremonese et al. 2020) during the photometric monitoring of comets (Table 4 and Fig. 3).

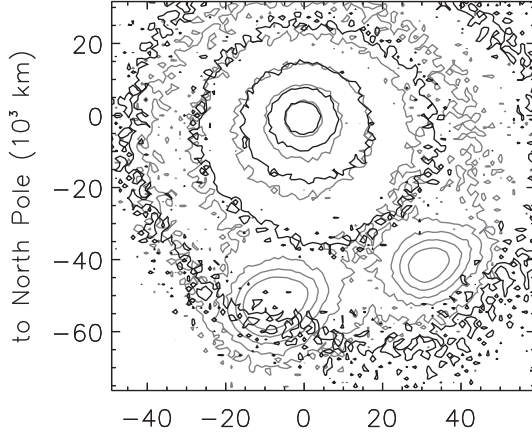


**Figure 4.** Isophotes of the observed (grey isophotes) and of the model (black isophotes) dust tail of comet C/2017K2 at  $r_h = 6.35$  au. The North direction is up, and the East direction to the left. The brightness step between isophotes is a factor two. The tail model assumes isotropic dust ejection from the nucleus, provides  $d = 0.175$  and is larger than observations on the western side.

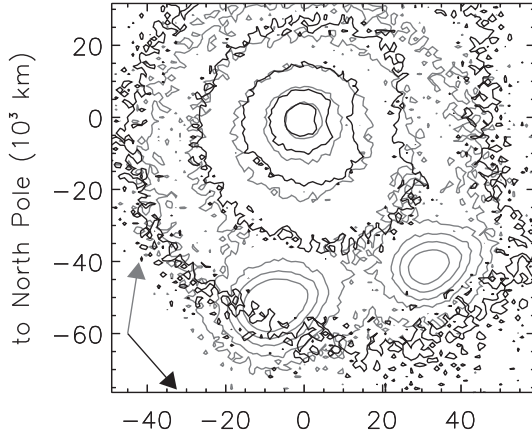


**Figure 5.** Isophotes of the observed (grey isophotes) and of the model (black isophotes) dust tail of comet C/2017K2 at  $r_h = 6.35$  au. Black arrow: antisolar direction. Grey arrow: trailing orbit direction. The tail model assumes no dust ejection from nucleus latitudes  $< -60$  deg, with a lower  $d = 0.165$ .

## 6 TAIL FITS AND RESULTS

Model tails of comets C/2017K2, C/2019O3, C/2020F2, C/2020H6, and C/2020R2 were obtained by means of Monte Carlo integration of  $3 \times 10^8$  particles following 3D heliocentric orbits fixed by the  $\beta$ -parameter and by the ejection velocity vector of absolute value  $v_d$  at  $r_h = 10$  au and depending on  $r_h^{-1}$ . We set the activity onset at 85 au (Table 2). The model tails were projected on the sky in images of  $100 \times 100$  pixels, with 1 pixel = 0.252 arcsec (TNG value). First, dust isotropic ejection was assumed, tuning the free parameters  $v_d$ ,  $\sigma$  and  $k$  to best fit tail photometry along its axis and the sunward coma (Figs 4–13). The best fit minimizes

$$d = \frac{2}{N} \sum_i^N \frac{(a_i - b_i)^2}{(a_i + b_i)^2}, \quad (10)$$

where  $a_i$  and  $b_i$  are the observed and model tail brightness sampled in  $N$  pixels, thus balancing the fits of tails and comae. Stars polluting the tails increase the  $d$ -values, thus explaining why they are a bit scattered (Table 5). The model fits the  $Af\rho$ -values measured in the tail images within the measurement errors. The observed tails showed

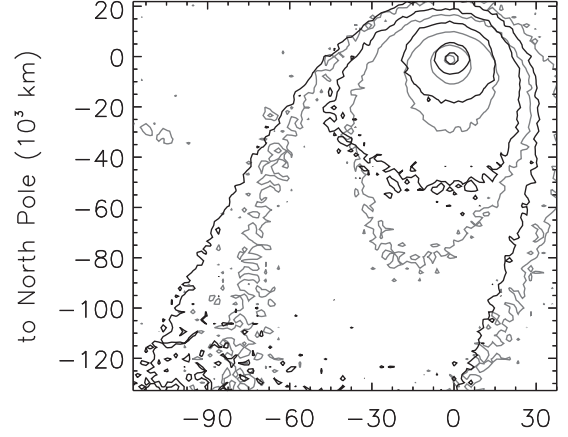


**Figure 6.** Isophotes of the observed (grey isophotes) and of the model (black isophotes) dust tail of comet C/2019O3 at  $r_h = 8.86$  au. The North direction is up, and the East direction to the left. The brightness step between isophotes is a factor three. The tail model assumes isotropic dust ejection from the nucleus, provides  $d = 0.108$  and is larger than observations on the eastern side.

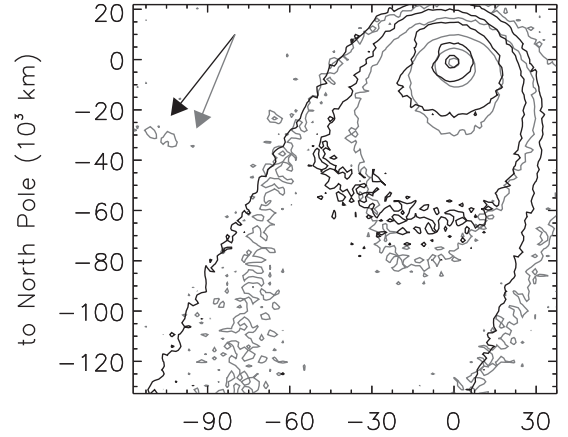


**Figure 7.** Isophotes of the observed (grey isophotes) and of the model (black isophotes) dust tail of comet C/2019O3 at  $r_h = 8.86$  au. Black arrow: antisolar direction. Grey arrow: trailing orbit direction. The tail model assumes no dust ejection from nucleus latitudes  $< -60$  deg, with a lower  $d = 0.081$ .

always asymmetries with respect to their axis, whose best fits require some anisotropy of dust ejection. Available data do not constrain the nucleus spin axis, so that we tested possible ejection anisotropies assuming a nucleus spin perpendicular to the comet orbital plane (zero obliquity case). This approach cannot provide the perfect fit of tail asymmetries, but can check if they are in fact due to the nucleus shape and seasons, if such an approach improves the fit with respect to the isotropic ejection. This is in fact the case for all five comets (Figs 4–13). As predicted by the activity model (Section 2), the anisotropies improving the fits were directed along nucleus latitudes, and never along the sunward-to-antisunward direction, consistent with chunks pushed into the inner-coma night side by rocket effects during the chunk erosion into sub-cm dust. Latitudinal anisotropies are inconsistent with enhanced activity on the sunward side of an isotropic nucleus, and point out a nucleus activity driven by the nucleus shape and seasons e.g. similar to 67P one.

Assuming that the here observed Oort comets of heliocentric orbital eccentricity  $e > 1$  (Table 3) approach the Sun for the first time, nucleus seasons driving cometary activity suggest that the

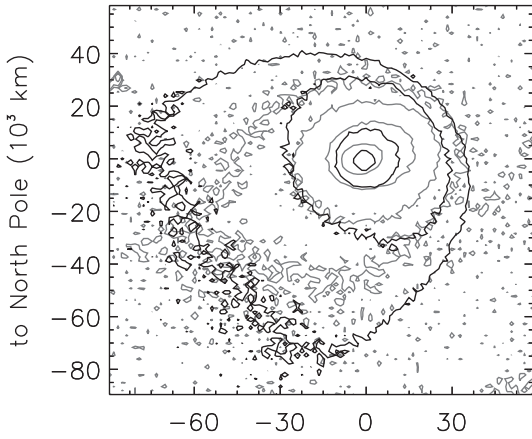


**Figure 8.** Isophotes of the observed (grey isophotes) and of the model (black isophotes) dust tail of comet C/2020F2 at  $r_h = 9.17$  au. The North direction is up, and the East direction to the left. The brightness step between isophotes is a factor three. The tail model assumes isotropic dust ejection, provides  $d = 0.148$  and is larger than observations on the northern and southern sides.

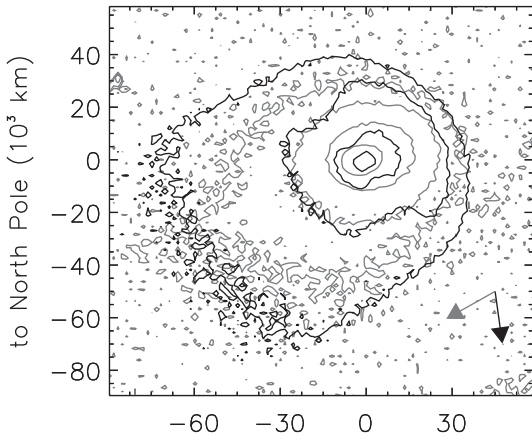


**Figure 9.** Isophotes of the observed (grey isophotes) and of the model (black isophotes) dust tail of comet C/2020F2 at  $r_h = 9.17$  au. Black arrow: antisolar direction. Grey arrow: trailing orbit direction. The tail model assumes no dust ejection from nucleus latitudes  $< -60$  and  $> +60$  deg, with a lower  $d = 0.122$ .

erosion of nuclei started as soon as the protoplanetary disc became transparent to solar radiation, because comets were probably born at  $r_h < 85$  au, i.e. at heliocentric distances where supervolatiles in the superficial pebbles necessarily trigger the nucleus erosion. For  $r_h > 20$  au, the computed  $E$  values (Table 2) provide an average erosion of  $1.5 \text{ m yr}^{-1}$ , and the computed  $v_d$  values (Table 2) are much lower than the escape velocity from nuclei larger than 1 km, thus implying local fallouts up to 100 m thick in less than a century (e.g. during the 60 yr spent today by all Oort nuclei along their inbound orbit from 85 to 4 au). The activity driven by supervolatiles differentiate the nucleus hemispheres by erosion on the polar summer and by fallout on the polar night of all nuclei having non-zero obliquity along a sector of their primordial orbit in the disc. Comets were ejected into the Oort cloud by close encounters with giant planets in fast inward migration (Pirani et al. 2019), surely avoiding any catastrophic collisions and any change of the primordial nucleus spin, because the nucleus erosion lifetime given by  $E$  is orders of magnitude shorter than the collisional lifetime (Fulle et al. 2020a).

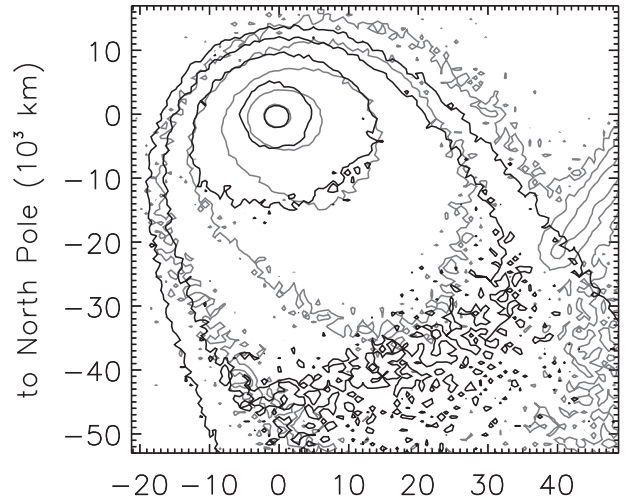


**Figure 10.** Isophotes of the observed (grey isophotes) and of the model (black isophotes) dust tail of comet C/2020H6 at  $r_h = 4.84$  au. The North direction is up, and the East direction to the left. The brightness step between isophotes is a factor three. The tail model assumes isotropic dust ejection from the nucleus, provides  $d = 0.143$  and is larger than observations on the eastern side.

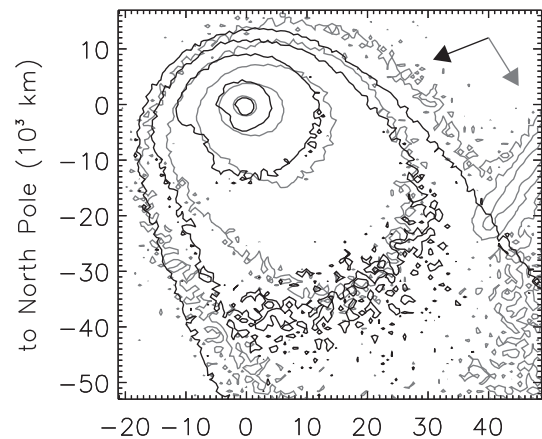


**Figure 11.** Isophotes of the observed (grey isophotes) and of the model (black isophotes) dust tail of comet C/2020H6 at  $r_h = 4.84$  au. Black arrow: antisolar direction. Grey arrow: trailing orbit direction. The tail model assumes no dust ejection from nucleus latitudes  $< -60$  deg, with a lower  $d = 0.115$ .

Table 5 lists the best-fitting parameters  $v_d$ ,  $\sigma$ , and  $k$ . Uniqueness tests performed on the model tails (see also fig. 4 in Cremonese et al. 2020) have shown that the tail size around its axis depends linearly on the dust velocity  $v_d$ , fixing its accuracy at 10 per cent of its values. The tail orientation depends on  $\sigma$  and drifts from the direction of the cometary trailing orbit to the antisolar direction as  $\sigma$  increases, suggesting an accuracy of 20 per cent of its values. Best fits of all tails were obtained assuming integer values of the  $k$  parameter, with  $k = 1$  providing long tails and  $k = 2$  providing short tails. The mean square errors of tail fits  $d$ , equation (10), did not appreciably decrease adopting non-integer  $k$ -values. As predicted by the activity model (Section 2), the  $v_d$ ,  $\sigma$  and  $k$  parameters show a strong correlation, which makes fast and robust the automation of tail fits in view of its application to the data set of the Vera Rubin LSST Survey. In particular, C/2017K2 is characterized by the largest parameters, and this fact explains why the tail of C/2017K2 is directed antisunward, whereas all the other four tails are directed along the trailing orbit.

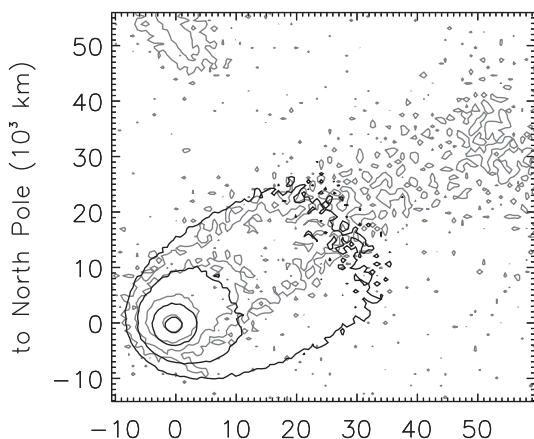


**Figure 12.** Isophotes of the observed (grey isophotes) and of the model (black isophotes) dust tail of comet C/2020R2 at  $r_h = 4.83$  au. The North direction is up, and the East direction to the left. The brightness step between isophotes is a factor three. The tail model assumes isotropic dust ejection from the nucleus, provides  $d = 0.073$  and is larger than observations on the southern side.

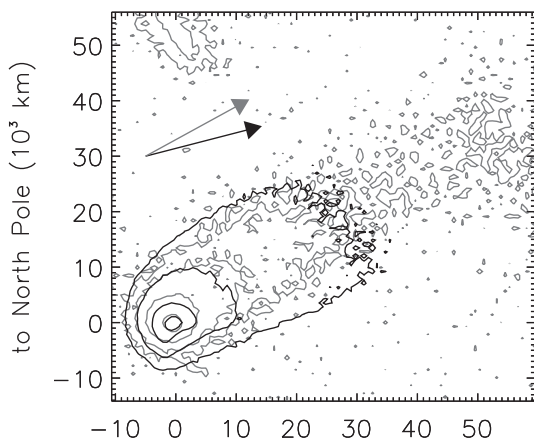


**Figure 13.** Isophotes of the observed (grey isophotes) and of the model (black isophotes) dust tail of comet C/2020R2 at  $r_h = 4.83$  au. Black arrow: antisolar direction. Grey arrow: trailing orbit direction. The tail model assumes no dust ejection from nucleus latitudes  $< -40$  deg, with a lower  $d = 0.057$ .

In fact, a steep loss rate ( $k > 1$ ) implies a dust tail mainly composed of dust ejected months before the tail observation, and a wide  $\beta$ -distribution [ $\sigma > 1.3$ , namely the value observed in water-driven 2I/Borisov at  $r_h \geq 2$  au (Cremonese et al. 2020)] implies the ejection of also small dust, pushed into the antisolar direction by the solar radiation pressure. On the contrary,  $k = 1$  implies a dust tail sensitive to dust ejected decades before the observations, and the low  $\sigma$ -values predicted by the activity model (Section 2) at  $r_h > 10$  au imply the ejection of mm-sized dust and larger, trailing the comet along its orbit. C/2020F2 is an intermediate case, with  $k = 2$  fitting the short tail, and  $\sigma < 1$  depleting the tail of small dust, so that it trails the comet orbit, although younger than those of C/2019O3, C/2020H6 and C/2020R2.

Combining the observed  $Af\rho$  with the best-fitting velocity  $v_d$ , we estimate the dust loss rate  $Q_d$  by means of equation (9), and the lower limit of the nucleus area  $A_d$  eroded into dust and chunks (Table 5) consistent with the predicted erosion  $E$  (Table 2),  $A_d = Q_d(\rho_d E)^{-1}$ . As predicted by the activity model (Section 2), C/2017K2 nucleus has a radius  $R_n > 2.5$  km, consistent with a dust velocity  $v_d =$

4 m s<sup>-1</sup>, twice that computed by the activity model assuming  $R_n = 1$  km, namely  $v_d \leq 2$  m s<sup>-1</sup> at  $r_h = 10$  au (Table 2). On the other side, the  $A_d$ -values of C/2019O3, C/1010F2 and C/2020H6 can be interpreted in two ways. The first is that a significant fraction of the nucleus of radius  $R_n > 1$  km is not active, so that the best fit at  $v_d \ll 2$  m s<sup>-1</sup> is due to a dominant nucleus gravity, dropping the ejection velocity of the low fraction of dust escaping the nucleus into the tail, while most dust falls back on the nucleus during all the inbound comet orbit. The second possible explanation considers a nucleus of radius  $R_n \leq 1$  km entirely active, consistent with a dust velocity  $v_d$  significantly lower than that computed in Table 2. Such a small nucleus may imply a small fallout, consistent with  $k = 1$ , the same  $r_h$ -dependence of nucleus erosion  $E$  (Section 2), whereas the large nucleus of C/2017K2 necessarily implies a large fallout. In fact, the C/2017K2 tail is best fit by  $k = 2$ , i.e. with  $Af\rho$  depending on  $r_h^{-1}$ , consistent with a dependence  $r_h^{-1.14}$  of the coma brightness (Jewitt et al. 2021) and with our observations of the time evolution of  $Af\rho$  (Fig. 3). Our values of  $A_d$  and of  $Q \leq 4 \times 10^{-6}$  kg m<sup>-2</sup> s<sup>-1</sup> at  $r_h = 6.7$  au and a depth  $s_c \geq 4$  cm (Table 2) are consistent with the measured CO loss rate of  $75 \pm 25$  kg s<sup>-1</sup> (Yang et al. 2021), which is lower than the computed CO<sub>2</sub> loss rate  $> 160$  kg s<sup>-1</sup> (Tables 2 and 5) and much lower than  $Q_d$ . It follows that all the differences observed among the five comets are probably due to their nucleus size only, consistent with the same activity driving all Oort comets as assumed in Section 2.

## 7 CONCLUSIONS

In this paper, we have started a statistical analysis of dust tails observed at heliocentric distances larger than 4 au, i.e. necessarily driven by the sublimation of ices more volatile than water-ice. We find that:

- (i) Dust tails are consistent with our activity model, based on the sublimation of ices always inside cometary porous dust particles.
- (ii) Therefore, Oort comets eject icy dust consistent with porous interplanetary dust particles and dust ejected by Jupiter family comets.
- (iii) Tail fits by means of the probabilistic tail model depend on three free parameters only, all correlated to the nucleus size.
- (iv) The differences among the observed Oort comets are probably due to the different size of the nucleus only, because at  $r_h > 4$  au the activity of comets depends on supervolatiles present in water-poor pebbles only. At  $r_h < 4$  au, different abundances of water-poor versus water-rich pebbles imply very different activity of comets having similar nucleus sizes (Fulle 2021).
- (v) In view of the analysis of the Vera Rubin LSST Survey data set, the automation of the probabilistic tail model is feasible.
- (vi) Tail fits are always improved by latitudinal anisotropies of the dust ejection, suggesting activity of nuclei dominated by seasons.
- (vii) Inbound seasons suggest cometary activity before the ejection of comets into the Oort cloud, as predicted by our activity model.
- (viii) Local fallout up to  $\approx 100$  m thick deposited during  $\approx 60$  yr inbound may cover Oort nuclei larger than 1 km.
- (ix) A dense cloud of bound dust is probable at  $r_h > 20$  au and implies overestimates of the nucleus sizes based on nuclear magnitudes or point-spread functions.
- (x) Oort nuclei smaller than 1 km may appear more pristine than Jupiter Family Comets when observed at 1 au from the Sun, although comet 103P/Hartley 2, with a nucleus of about 1 km size (Lis et al. 2019), shows thick deposits as well.

**Table 5.** Dust and nucleus parameters.  $v_d$ : Dust ejection velocity ( $\text{m s}^{-1}$ ) at the reference values  $\beta_0$  and  $r_h = 10$  au.  $d_1$  and  $d_2$ : Mean square error of the fit in case of isotropic and anisotropic dust ejection, respectively, equation (10).  $Af\rho$ : Coma brightness (m, Table 4 and Fig. 3) converted to the reference heliocentric distance  $r_h = 10$  au according to the index  $k$ .  $Q_d$ : Dust loss rate ( $\text{kg s}^{-1}$ ) at the reference heliocentric distance  $r_h = 10$  au, equation (9).  $A_d$ : Lower limit of the nucleus surface ( $\text{km}^2$ ) eroded into dust,  $A_d = Q_d(\rho_d E)^{-1}$ , assuming  $\rho_d = 800 \text{ kg m}^{-3}$  (Fulle et al. 2017). The larger the fallout, the larger the eroded nucleus surface with respect to  $A_d$ .  $R_n$ : Lower limit of the nucleus radius (km),  $R_n = \sqrt{A_d/\pi}$ .

Comet	$v_d$	$\sigma$	$k$	$d_1$	$d_2$	$Af\rho$	$Q_d$	$A_d$	$R_n$
C/2017K2	4.0	1.8	2	0.175	0.165	$53 \pm 10$	$4250 \pm 800$	$>20 \pm 5$	$>2.5 \pm 0.3$
C/2019O3	0.7	0.5	1	0.108	0.081	$50 \pm 10$	$700 \pm 150$	$\geq 3 \pm 1$	$\geq 1.0 \pm 0.1$
C/2020F2	0.9	0.5	2	0.148	0.122	$30 \pm 5$	$550 \pm 100$	$>2.6 \pm 0.5$	$>0.9 \pm 0.1$
C/2020H6	0.5	0.5	1	0.143	0.115	$7.5 \pm 1.0$	$75 \pm 10$	$\geq 0.3 \pm 0.1$	$\geq 0.3 \pm 0.05$
C/2020R2	0.4	0.7	1	0.073	0.057	–	–	–	–

(xi) Unlike Jupiter family comets, the ejection of sub-cm dust from Oort comets at 1 au may be driven also by supervolatiles.

## ACKNOWLEDGEMENTS

We thank two anonymous referees for having significantly improved the paper. Part of this research was supported by the ESA Express Procurement (EXPRO) RFP for IPL-PSS/JD/190.2016, by the Italian Space Agency (ASI) within the ASI-INAF agreements I/032/05/0 and I/024/12/0, and by the ISSI Team 533 ‘Characterization of the Transition from Supervolatiles-Driven Activity to Water-Driven Activity in inbound Dynamically New Comets’ led by F. La Forgia.

## DATA AVAILABILITY

The data underlying this paper are available in the given references and upon request.

## REFERENCES

A’Hearn M. F. et al., 1984, *AJ*, 89, 579  
 Ahern J. E., Lawson T. W., Jr., 1968, Cryogenic Solid Oxygen Storage and Sublimation Investigation, DTIC Document  
 Balucani N., Ceccarelli C., Taquet V., 2015, *MNRAS*, 449, L16  
 Blum J., Gundlach B., Mühle S., Trigo-Rodrigues J., 2014, *Icarus*, 235, 156  
 Blum J. et al., 2017, *MNRAS*, 469, S755  
 Bertini I. et al., 2019, *MNRAS*, 482, 2924  
 Bouziani N., Jewitt D., 2022, *ApJ*, 924, 37  
 Brisset J., Heisselmann D., Kothe S., Weidling R., Blum J., 2016, *A&A*, 593, A3  
 Brownlee D. et al., 2006, *Science*, 314, 1711  
 Cambianica P. et al., 2020, *A&A*, 636, A91  
 Ciarniello M. et al., 2021, 52nd Lunar and Planet. Sci. Conf., LPI Contribution, Vol. 2548. The Woodlands, TX, p. 2031  
 Ciarniello M. et al., 2022, *Nat. Astron.*, 6, 546  
 Cremonese G. et al., 2020, *ApJ*, 893, L12  
 Dymock R., Miles R., 2018, *J. British Astron. Assoc.*, 128, 347  
 Davidsson B. J. R., Samarasingha N. H., Farnocchia D., Gutierrez P. J., 2022, *MNRAS*, 509, 3065  
 Fornasier S. et al., 2015, *A&A*, 583, A30  
 Fray N., Schmitt B., 2009, *Planet. Space Sci.*, 57, 2053  
 Fulle M., 2021, *MNRAS*, 505, 3107  
 Fulle M., Blum J., 2017, *MNRAS*, 469, S39  
 Fulle M. et al., 2010, *A&A*, 522, A63  
 Fulle M. et al., 2016, *ApJ*, 821, 19  
 Fulle M. et al., 2017, *MNRAS*, 469, S45  
 Fulle M., Blum J., Rotundi A., 2019, *ApJ*, 879, L8  
 Fulle M., Blum J., Rotundi A., 2020a, *A&A*, 636, L3

Fulle M., Blum J., Rotundi A., Gundlach B., Güttler C., Zakharov V. V., 2020b, *MNRAS*, 493, 4039  
 Gundlach B., Blum J., Keller H. U., Skorov Y. V., 2015, *A&A*, 583, A12  
 Gundlach B., Fulle M., Blum J., 2020, *MNRAS*, 493, 3690  
 Güttler C. et al., 2019, *A&A*, 630, A24  
 Henden A. A., Templeton M., Terrell D., Smith T. C., Levine S., Welch D., 2016, American Astronomical Society, AAS Meeting #225, id.336.16  
 Holmberg J., Flynn C., Portinari L., 2006, *MNRAS*, 367, 449  
 Huebner W. F. et al., 2006, Heat and Gas Diffusion in Comet Nuclei (ISBN 1608-280X, Published for The International Space Science Institute, Bern, Switzerland). ESA Publ. Division, Noordwijk, the Netherlands  
 Jewitt D., Hui M.-T., Mutchler M., Weaver H., Li J., Agarwal J., 2017, *ApJ*, 847, L19  
 Jewitt D., Kim Y., Mutchler M., Agarwal J., Li J., Weaver H., 2021, *AJ*, 161, 188  
 Jones R. L. et al., 2020, preprint(<https://arxiv.org/pdf/2009.07653.pdf>)  
 Kelley M. S. P. et al., 2013, *Icarus*, 225, 475  
 Kelley M. S. P. et al., 2015, *Icarus*, 262, 187  
 Keller H. U. et al., 2015, *A&A*, 583, A34  
 Landolt A. U., 2009, *AJ*, 137, 4186  
 Läuter M., Kramer T., Rubin M., Altwegg K., 2020, *MNRAS*, 498, 3995  
 Levasseur-Regourd A.-C. et al., 2018, *Space Sci. Rev.*, 214, 64  
 Lis D. C. et al., 2019, *A&A*, 625, L5  
 Mannel T. et al., 2019, *A&A*, 630, A26  
 Meech K. J. et al., 2013, *Icarus*, 222, 662  
 Müller D. R. et al., 2022, *A&A*, in press  
 Ott T. et al., 2017, *MNRAS*, 469, S276  
 Pajola M. et al., 2017, *MNRAS*, 469, S636  
 Pirani S., Johansen A., Bitsch B., Mustill A. J., Turrini D., 2019, *A&A*, 623, A169  
 Regnier J., 1972, *J. Chim. Phys.-Chim. Biol.*, 6, 942  
 Rubin M. et al., 2020, *Space Sci. Rev.*, 216, 102  
 Shulman L. M., 2004, *A&A*, 416, 187  
 Skorov Y. V., Blum J., 2012, *Icarus*, 221, 1  
 Skorov Y. V., Keller H. U., Mottola S., Hartogh P., 2020, *MNRAS*, 494, 3310  
 Snodgrass C., Jones G. H., 2019, *Nat. Commun.*, 10, 5418  
 Stephenson R. M., Melinowski S., 1987, Handbook of Thermodynamics of Organic Compounds. Springer, Berlin  
 Takahashi Y., Westrum E. F., Jr., 1970, *J. Chem. Thermodyn.*, 2, 847  
 Yang B., Jewitt D., Zhao Y., Jiang X., Ye Q., Chen Y.-T., 2021, *ApJ*, 914, L17  
 Zacharias N., Funch C. T., Girard T. M., Henden A., Bartlett J. L., Monet D. G., Zacharias M. I., 2013, *AJ*, 145, 44  
 Zakharov V. V., Ivanovski S. L., Crifo J. F., Della Corte V., Fulle M., Rotundi A., 2018, *Icarus*, 312, 121  
 Zakharov V. V., Rotundi A., Della Corte V., Ivanovski S. L., Rodionov A. V., Bykov N. Y., 2021, *Icarus*, 364, 114476

This paper has been typeset from a  $\text{\TeX}/\text{\LaTeX}$  file prepared by the author.